Acid-Treatment-Assisted Liquid Metal–Based Zinc Metal Anode for Stable Aqueous Zinc-Ion Batteries

Citation for the original published paper (version of record):

Yoon, H., Choi, C., Hong, S. et al (2025). Acid-Treatment-Assisted Liquid Metal–Based Zinc Metal
Anode for Stable Aqueous Zinc-Ion
Batteries. International Journal of Energy Research, 2025(1). http://dx.doi.org/10.1155/er/1405163

N.B. When citing this work, cite the original published paper.

(article starts on next page)

WILEY

Research Article

Acid-Treatment-Assisted Liquid Metal–Based Zinc Metal Anode for Stable Aqueous Zinc-Ion Batteries

Hyungsub Yoon [iD],[1] **Chunghyeon Choi** [iD],[1] **Seungwoo Hong** [iD],[2] **Marita Afiandika**,[3] **Aleksandar Matic** [iD],[3,4] **Tae Gwang Yun** [iD],[5] and **Byungil Hwang** [iD][2]

[1]*Department of Intelligent Semiconductor Engineering, Chung-Ang University, Seoul 06974, Republic of Korea*
[2]*School of Integrative Engineering, Chung-Ang University, Seoul 06974, Republic of Korea*
[3]*Department of Physics, Chalmers University of Technology, Gothenburg 41296, Sweden*
[4]*Wallenberg Wood Science Center, Department of Physics, Chalmers University of Technology, Gothenburg 41296, Sweden*
[5]*Department of Molecular Science and Technology, Ajou University, Suwon 16499, Republic of Korea*

Correspondence should be addressed to Aleksandar Matic; matic@chalmers.se, Tae Gwang Yun; ytk0402@ajou.ac.kr, and Byungil Hwang; bihwang@cau.ac.kr

Aqueous Zn-ion batteries (AZIBs) are considered to be a promising alternative to Li-ion batteries (LIBs) owing to the low cost, superior safety, and high theoretical capacity of the Zn anode ($820 \, \mathrm{mAh \, g^{-1}}$ and $5855 \, \mathrm{mAh \, cm^{-3}}$). However, Zn metal anodes encounter challenges, mainly including the formation of unfavorable byproducts and the growth of Zn dendrites. Furthermore, Zn metal corrosion and the hydrogen evolution reaction (HER) are issues related to AZIBs. To overcome these issues, we engineered a Zn metal surface using acid treatment and eutectic GaIn–liquid metal (EGaIn–LM) coating. Coating EGaIn–LM on the Zn metal anode results in an liquid–liquid interface between the electrolyte and electrode, increasing wettability and accelerating charge transfer kinetics, with respect to a bare Zn metal anode. Furthermore, the EGaIn–LM coating improved corrosion resistance and reduced the HER owing to the high overpotentials of the reaction with Ga and In. Based on these advantages, EGaIn–LM@acidified Zn (EGaIn–LM@AZn) anodes showed stable symmetric cycling over 420 h and exhibited high stability against the formation of byproducts and Zn dendrites. Finally, we prepared V_2O_5 cathode–based full cells with different anodes. The V_2O_5//EGaIn–LM@AZn full cell demonstrated excellent rate capability, long-term charge/discharge cycling (capacity retention of 71.8% after 1500 cycles at a current density of $5 \, \mathrm{A \, g^{-1}}$), and high specific capacities under various current densities owing to improved charge transfer kinetics and the protective nature of EGaIn–LM. The proposed simple EGaIn–LM coating method may offer a promising strategy to prepare a stable Zn anode.

Keywords: aqueous Zn-ion batteries; dendrite-free; eutectic GaIn; interface engineering; liquid metal; Zn metal anode

1. Introduction

Rechargeable batteries are increasingly important in applications ranging from portable electronics to electric vehicles and grid storage systems [1–3]. Currently, the Li-ion battery (LIB) dominates the battery market share due to their high energy density and durability [4]. However, LIBs encounter significant challenges, including safety concerns, high costs, and limited resource availability [5]. Aqueous Zn-ion batteries (AZIBs) have emerged as promising alternatives, offering advantages such as environmental friendliness, safety through aqueous electrolytes, cost-effectiveness, and greater stability [6, 7]. Furthermore, they also provide a favorable redox potential ($-0.76 \, \mathrm{V}$ vs. standard hydrogen electrode (SHE)) and potential for high theoretical capacity related to the Zn anode (820 and $5855 \, \mathrm{mAh \, cm^{-3}}$). Despite these benefits, AZIBs suffer from certain challenges such as dendrite growth during plating and stripping, byproduct formation, Zn metal corrosion,

hydrogen evolution reaction (HER), and formation of passivation layers, all of which degrade electrochemical performance, leading to delaying commercialization of AZIBs [8, 9].

These challenges have been addressed through various strategies, including a protective coating layer [10–12], a structural design on Zn anode [13, 14], a use of electrolyte additives or hydrogel electrolyte [15, 16], a separator design [17, 18], et cetera [19, 20]. Among them, the protective coating layer on Zn anode is a relatively simple and effective strategy to suppress dendrite growth and protect the Zn anode from corrosion and HER [21–23]. Previous studies have introduced protective layers composed of polymers [24, 25], metal–organic frameworks [26, 27], and conductive materials [28, 29]. However, they have encountered challenges, including low ionic conductivity, complex synthesis process, and toxicity concerns. Therefore, it is essential to develop new coating materials that effectively regulate unfavorable dendrite and byproduct formation and ensure environmental friendliness and scalability for practical applications [30].

Recently, eutectic GaIn–liquid metal (EGaIn–LM) has shown promise as an effective coating material. First, due to its liquid-to-liquid interface with the electrolyte, it is able to reduce interfacial charge and mass transfer resistances of Zn anode [31]. Second, it is potential to suppress dendrite growth because of strong affinity to Zn and a low energy barrier for Zn-ion migration [32]. Third, the EGaIn–LM layer prevents anode corrosion and passivation caused by the HER owing to the high overpotentials of Ga (Ga^{3+}/Ga (−0.53 V vs. SHE)) and In (In^{3+}/In (−0.34 V vs. SHE)) [33, 34]. However, it is difficult to coat EGaIn–LM on Zn anode due to its high surface tension ($0.624\ N\ m^{-1}$) [35, 36]. Previous studies have primarily employed mechanical polishing to enhance the wettability of EGaIn–LM on Zn anode [33, 37]. However, this approach increases surface roughness, adversely affecting the cycling stability of AZIBs. Therefore, an alternative method to increase the wettability while retaining a low surface roughness is urgently required.

In this study, we suggested a novel approach combining chemical acid etching and EGaIn–LM coating to enhance wettability of EGaIn–LM and electrochemical stability of Zn anode. The acid treatment effectively removes undesirable passivation layer and Zn crystal planes of Zn metal [22, 38]. We investigated electrochemical performance of symmetric cells with bare Zn, acidified Zn (AZn), and EGaIn–LM coated AZn (EGaIn–LM@AZn). Additionally, the electrochemical performances of V_2O_5 cathode–based full cells containing three different anodes have been explored.

2. Materials and Methods

2.1. Materials. All chemicals were used without further purification. The precursors of EGaIn–LM, Ga, and In were purchased from Ruichi Metals. Zn (0.25 mm thick) and Ti foil (0.032 mm thick) were purchased from Thermo Fisher. V_2O_5, the cathode active material, and Zn sulfate heptahydrate ($ZnSO_4$), an electrolyte salt, were purchased from Duksan. Super P and PVDF, a conductive material and a binder, respectively, were purchased from MTI Korea. Glass fiber, a

separator, was purchased from Hyundai Micro, and N-methyl-2-pyrrolidone (NMP) was purchased from Samchun. To acid treat Zn, sulfuric acid (H_2SO_4) purchased from Daejung was used.

2.2. Preparation of the Electrodes. For preparing the EGaIn-coated Zn anode, EGaIn–based LM ink (Ga: 74.5 wt% and In: 25.5 wt%) was prepared by mixing Ga and In at 200°C for 20 h. A Zn anode with a diameter of 12 mm was repeatedly washed with ethanol and dried at 60°C for 15 min. Subsequently, the dried Zn was immersed in a 0.5 M aqueous solution of H_2SO_4, ultrasonicated for 30 min, and subsequently dried at 60°C for 30 min. After acidification, EGaIn–based LM was applied to the surface of Zn by simple brush coating. We denoted EGaIn–based LM-coated AZn as EGaIn@AZn. To verify the effect of the acification and EGaIn-LM coating on the Zn metal, we also utilized bare Zn and AZn as the control group. The V_2O_5 cathodes were prepared by mixing materials, including V_2O_5, carbon black, and PVDF, that is, the active material, conductive material, and binder, respectively, in a 7:2:1 weight ratio and subsequently dispersing in NMP to obtain a homogeneous slurry. The slurry was cast on the Ti foil using the doctor blade method and subsequently dried at 80°C in vacuum for 24 h. The areal mass loading of the cathode was between $0.8–1.0\ mg\ cm^{-2}$.

2.3. Electrochemical Characterization. All electrochemical measurements were conducted using 2032 coin-type cells with 160 μL of a 2 M $ZnSO_4$ aqueous solution and a GF separator. The cathodes and anodes were punched with a diameter of 12 mm. Various electrochemical tests, including the galvanostatic cycling of the symmetric cell, cyclic voltammetry (CV), charge–discharge, and electrochemical impedance spectroscopy (EIS), were conducted using a battery tester (BCS-805, BioLogic). The EIS analysis was conducted on the cells at a frequency range of 10 kHz to 100 mHz with an applied voltage amplitude of 10 mV. Coulombic efficiency (CE) and chronoamperometry (CA) tests were conducted using a ZIBE SP1, WonATech, battery tester. The CE measurements were conducted on 2023 coin-type cells assembled with Cu//Zn, Cu//AZn, and Cu//EGaIn–LM@AZn in asymmetric cells at a current density of $1\ mA\ cm^{-2}$ with an areal capacity of $1\ mAh\ cm^{-2}$. The CA tests were conducted at −150 mV to investigate the two- and three-dimensional diffusion of Zn ions of the Zn anodes. For linear sweep voltammetry (LSV) and Tafel tests, three different typed Zn anodes were investigated using a three-electrode system (SP-150e, BioLogic). For these tests, the Zn anodes ($1 \times 1\ cm^2$), a Pt electrode, and Ag/AgCl (filled with saturated KCl) were used as the working electrode, the counter electrode, and the reference electrode, respectively. LSV was conducted to investigate the HER of the each Zn anode in 1 M Na_2SO_4 at a $5\ mV\ s^{-1}$ rate. For HER investigations, we used 1 M Na_2SO_4 electrolyte, instead of 2 M $ZnSO_4$ electrolyte, due to the elimination of the interference of Zn ion deposition process during tests [39]. Tafel tests were conducted to measure the corrosion resistances of each Zn anode in a 2 M $ZnSO_4$ electrolyte under a $1\ mV\ s^{-1}$ rate. Full cell tests (V_2O_5//bare Zn, V_2O_5//AZn, and V_2O_5//EGaIn–LM@AZn) were conducted under a voltage range of 0.2–1.6 V (vs. Zn/Zn^{2+}).
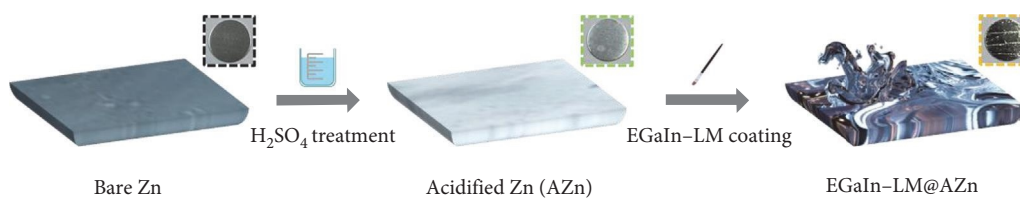
FIGURE 1: Schematic of the fabrication process of EGaIn–LM@AZn (inset images: photos of bare Zn, AZn, and EGaIn–LM@AZn).

2.4. Characterization. The surface morphologies of the bare Zn, AZn, and EGaIn–LM@AZn anodes were investigated via field-emission scanning electron microscopy (FE-SEM; SIGMA300, Carl Zeiss AG). In addition, each Zn anode was tested after soaking in electrolyte for 10 days and cycling over 20 cycles at a current density of $1\,mA\,cm^{-2}$ with an areal capacity of $1\,mAh\,cm^{-2}$ to investigate the stability against the byproduct and the dendrites on the surface. The X-ray diffraction (XRD) patterns of the pristine, soaked, and cycled anodes were recorded in the 2θ range of $5°$–$80°$ using Cu–Kα radiations to investigate the formation of a byproduct and dendrites by recording under a scan rate of $5°\,min^{-1}$ (New D8-Advance, Bruker-AXS). The contact angles of the Zn, AZn, and EGaIn–LM@AZn anodes were determined using $2\,M$ ZnSO$_4$ using a drop shape analyzer (DSA-100, KRUSS).

3. Results and Discussion

The fabrication process of the EGaIn–LM@AZn anode is schematically depicted in Figure 1. Zn was immersed in a $0.5\,M$ aqueous solution of H$_2$SO$_4$ for 30 min in a sonication bath to smoothen the Zn surface. After acid treatment, EGaIn–LM was applied to AZn via a simple brushing process. The photographs in Figure 1 show that EGaIn–LM is uniformly coated on AZn. However, without acid treatment, the Zn surface was difficult to coat due to the poor wettability (Figure S1). To study the effects of acid treatment and the presence of EGaIn–LM on the electrochemical performances, we prepared conventional Zn, AZn, and EGaIn–LM@AZn electrodes.

First, we obtained the CA profiles of the three anodes. Comparing the profiles (Figure 2a) obtained at $-150\,mV$ of three typed Zn anodes revealed that the current density rapidly flattened within approximately $10\,s$ with the EGaIn–LM@AZn anode, indicating that EGaIn–LM effectively constrained the diffusion of Zn^{2+} and restricted the growth of dendrites [40]. Corrosion resistance was determined via Tafel tests conducted in $2\,M$ ZnSO$_4$. As shown in Figure 2b, EGaIn–LM@AZn exhibited the highest corrosion potential ($-982.7\,mV$), followed by AZn ($-985.5\,mV$) and bare Zn ($-996.5\,mV$). A high corrosion potential and low corrosion rate indicate that the electrode is stable against corrosion by the electrolyte, indicating that EGaIn–LM coating and acid treatment positively affects the Zn anode. Furthermore, we conducted LSV tests in a $1\,M$ Na$_2$SO$_4$ electrolyte to evaluate the HER. As shown in Figure 2c, EGaIn–LM@AZn exhibits significantly low onset potential for the HER ($-2.2\,V$ at $-20\,mA\,cm^{-2}$), whereas the onset potentials exhibited by the bare Zn and AZn anodes were -1.89 and $-2.1\,V$ at a current density of $-20\,mA\,cm^{-2}$, respectively. These results can be attributed to EGaIn–LM acting as the passivation layer to prevent direct contact with the electrolyte and the high overpotentials of Ga (Ga^{3+}/Ga ($-0.53\,V$ vs. SHE)) and In (In^{3+}/In ($-0.34\,V$ vs. SHE)). In addition, owing to EGaIn–LM present in the liquid state, liquid-to-liquid contact was formed at the interface of the EGaIn–LM@AZn anode and the electrolyte, instead of solid-to-liquid contact under general situations. This unique interface ensured rapid mass transfer kinetics and delayed the corrosion of Zn. Moreover, the wettability of the anode to the electrolyte was enhanced, effectively improving electrochemical performance. Therefore, to investigate the effect of EGaIn–LM on the wettability of the anode, we conducted contact angle measurements by dropping a $2\,M$ ZnSO$_4$ electrolyte on the anodes (Figure S2). The bare Zn anode exhibited a contact angle of $72.5°$, whereas AZn exhibited a contact angle of $60.5°$ owing to the etching effect of acid treatment on the Zn surface. Unlike bare Zn and AZn, after the introduction of EGaIn–LM, the contact angle of the anode decreased significantly to $5.5°$ owing to liquid-to-liquid contact, imparting rapid charge transfer kinetics. Therefore, we verified the low charge transfer resistance of EGaIn–LM@AZn via EIS analysis (Figure 2d). As shown in Figure 2d, the charge transfer resistance of EGaIn–LM@AZn was much lower than those of bare Zn and AZn, consistent with the contact angle trends. Based on these results, EGaIn–LM@AZn coating may be considered a promising strategy to improve the stability of Zn anodes.

Nucleation overpotential is a key index for investigating Zn plating behavior. During the nucleation process, a reduced nucleation overpotential indicates a reduced resistance to nucleation, indicating the benefit of reducing energy consumption [41, 42]. To evaluate the nucleation overpotentials of the three anodes, we implemented a galvanostatic Zn electroplating process on each sample at a current density of $1\,mA\,cm^{-2}$ with an areal capacity of $1\,mAh\,cm^{-2}$. As shown in Figure 3a, EGaIn–LM@AZn exhibits the lowest nucleation overpotential ($20.4\,mV$), whereas AZn and bare Zn exhibits nucleation overpotentials of 34.7 and $122.3\,mV$, respectively. This indicates that acid treatment and EGaIn–LM coating reduced the Zn plating barrier and accelerated Zn^{2+} transfer kinetics, indicating homogeneous Zn nucleation and deposition. Moreover, we tested the galvanostatic long-term cycling stability of the anodes at a current density of $1\,mA\,cm^{-2}$ with an areal capacity of $1\,mA\,cm^{-2}$ (Figure 3b). Figure 3b displays that bare Zn and AZn fail within 66 and $115\,h$, respectively. In contrast, EGaIn–LM@AZn maintained a stable Zn plating/stripping performance over $420\,h$, substantially longer than bare Zn and AZn, indicating that EGaIn–LM restricted the formation of unfavorable byproducts and dendrite growth. We summarized the galvanostatic long-term cycling stability of Zn anode
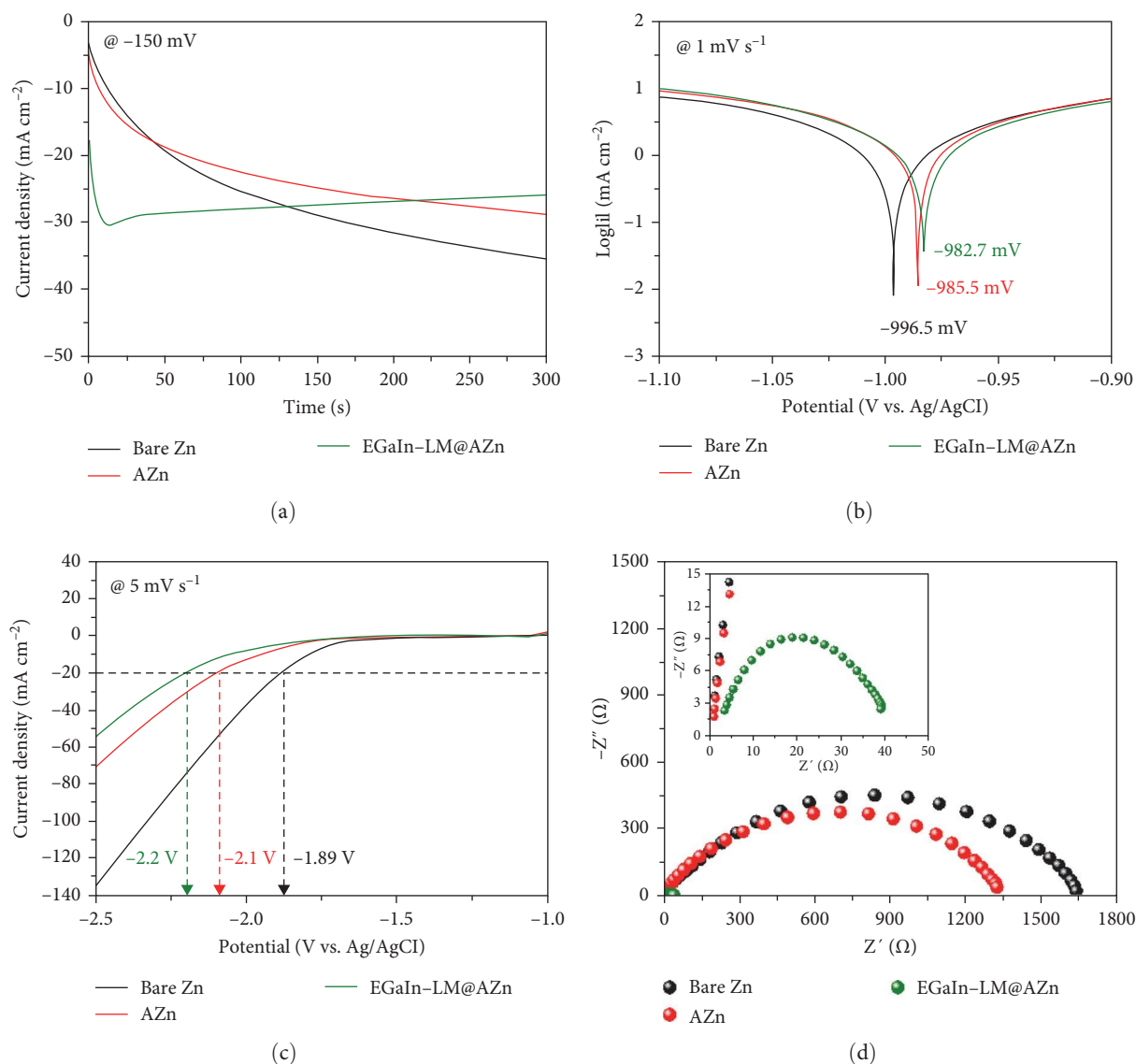
FIGURE 2: Electrochemical characterizations of the bare Zn, AZn, and EGaIn–LM@AZn anodes. (a) Chronoamperometry measurements, (b) Tafel tests, (c) LSV measurements, and (d) EIS analysis.
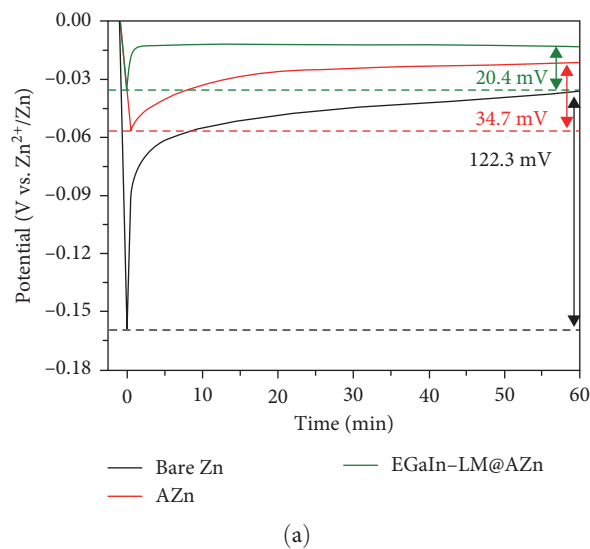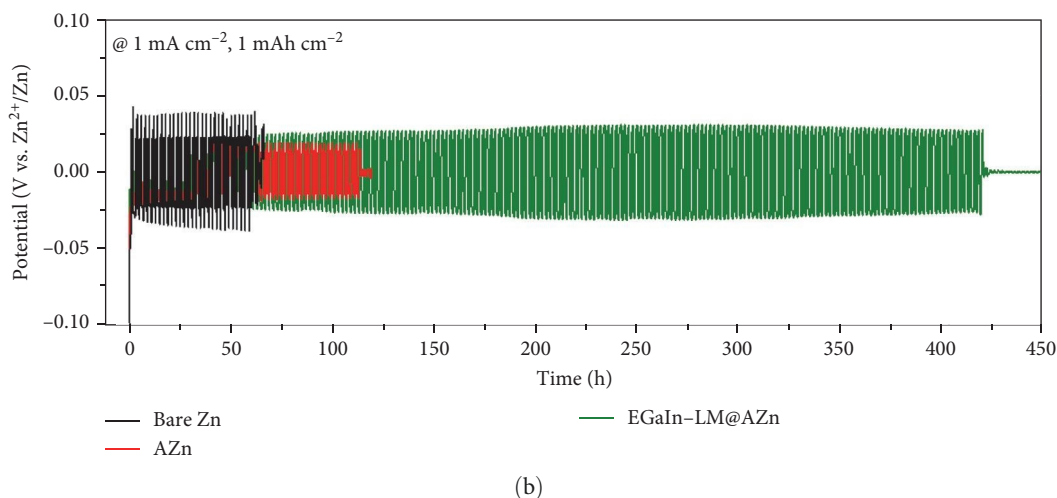

(a)

FIGURE 3: Continued.

(b)

FIGURE 3: (a) Nucleation overpotential profiles and (b) galvanostatic long-term cycling stabilities of the bare Zn, AZn, and EGaIn–LM@AZn anodes at a current density of $1\,mA\,cm^{-2}$ with an areal capacity of $1\,mAh\,cm^{-2}$.

with various coating materials (Table S1). The strategy of coating EGaIn–LM on AZn achieved comparable or longer cycling stability without a complicate process, compared to Zn anode with different coating materials. Therefore, this strategy was demonstrated as a promising and efficient method to restrict the formation of byproducts and dendrite growth.

To clarify the effect of acid treatment and EGaIn–LM coating on Zn, XRD patterns and SEM images of the three types of anodes were acquired, and the anodes were characterized after soaking for 10 days and cycling 20 times at a current density of $1\,mA\,cm^{-2}$ with an areal capacity of $1\,mAh\,cm^{-2}$. Generally, the XRD patterns of Zn revealed that the Zn (002) plane, instead of the Zn (100) and Zn (101) planes, was parallelly aligned to the substrate, alleviating unfavorable Zn growth [43]. As shown in Figure 4a, after acid treatment, the intensity of the Zn (002) peak is higher than that of the Zn (100) peak, indicating that the acid treatment etches unfavorable Zn (100), in contrast with the case of the bare Zn anode. In the case of EGaIn–LM@AZn, the intensity of the Zn (002) peak was also observed to be higher than the Zn (100) peak. Furthermore, after EGaIn–LM coating on the AZn anode, a broad XRD peak appeared between 30°–40°, confirming that EGaIn–LM successfully covered the AZn anode surface (Figure S3) [44]. Figure 4b displays the XRD patterns of three different anodes after soaking in a 2 M ZnSO₄ electrolyte for 10 days to investigate the inevitable formation of byproducts, known as Zn hydroxide sulfate (ZHS). After soaking in the electrolyte, the surfaces of all three anodes yielded new XRD peaks at approximately 10°, one of the main peaks of $Zn_4(OH)_6SO_4\cdot5H_2O$ [45]. Notably, the intensity of the ZHS peak obtained from the EGaIn–LM@AZn anode was much lower than that of the bare Zn and AZn anodes, indicating that EGaIn–LM increased the resistance to the formation of ZHS byproducts and acted as an effective protective layer. Moreover, we acquired the XRD patterns after 20 cycling tests at $1\,mA\,cm^{-2}$ with an areal capacity of $1\,mAh\,cm^{-2}$ (Figure 4c). After the cycling tests, the intensity corresponding to Zn (100) of the cycled bare Zn anode

increased significantly, indicating that the Zn dendrite grew vertically. Similarly, the intensity of the Zn (002) peak obtained from the pristine AZn anode was higher than that of the Zn (100) peak; however, the intensity of the Zn (002) peak obtained from the cycled AZn anode was lower than that of the Zn (100) peak. This indicated that the Zn (100) plane, instead of the Zn (002) plane, was predominantly formed. However, the Zn (002), Zn (100), and Zn (101) peaks in the XRD patterns of cycled EGaIn–LM@AZn showed negligible differences to those of pristine EGaIn–LM@AZn. To further confirm the intensity changes of Zn (002) and Zn (100), we calculated the intensity ratios of Zn (002) and Zn (100) of the pristine and cycled anodes, widely used to evaluate the growth plane of the Zn dendrites [46]. Figure 4d reveals that the intensity ratio ($I_{(002)}/I_{(101)}$) of bare Zn before and after the cycling test changes from 0.24 to 0.22 and that of AZn changes from 1.78 to 0.77. However, the intensity ratios of EGaIn–LM@AZn before and after the cycling tests increased from 1.11 to 1.39, indicating that a more stable Zn (002) plane was predominantly formed, instead of a stable Zn (100) plane, rendering EGaIn–LM@AZn more stable than the other two anodes during the galvanostatic cycling tests. Next, we acquired the SEM images of the anodes. Figure S4 displays the SEM image of the pristine bare Zn, AZn, and EGaIn–LM@AZn anodes. Figure S4a–c reveals that the surface of AZn is smoother than that of bare Zn because acid treatment etched the Zn surface. Moreover, after EGaIn–LM coating on AZn, the surface became clean, indicating that EGaIn–LM effectively covered the AZn surface. However, the SEM images obtained after soaking bare Zn in the electrolyte revealed that the surface contained large vertically grown ZHS byproducts, consistent with the XRD results obtained from soaked bare Zn (Figure S5a). Although ZHS byproducts were present on soaked AZn, their sizes were much smaller than those of soaked bare Zn (Figure S5b), indicating that acid treatment enhanced the resistance to the formation of ZHS byproducts. However, the surface of soaked EGaIn–LM@AZn contained reduced amounts of ZHS
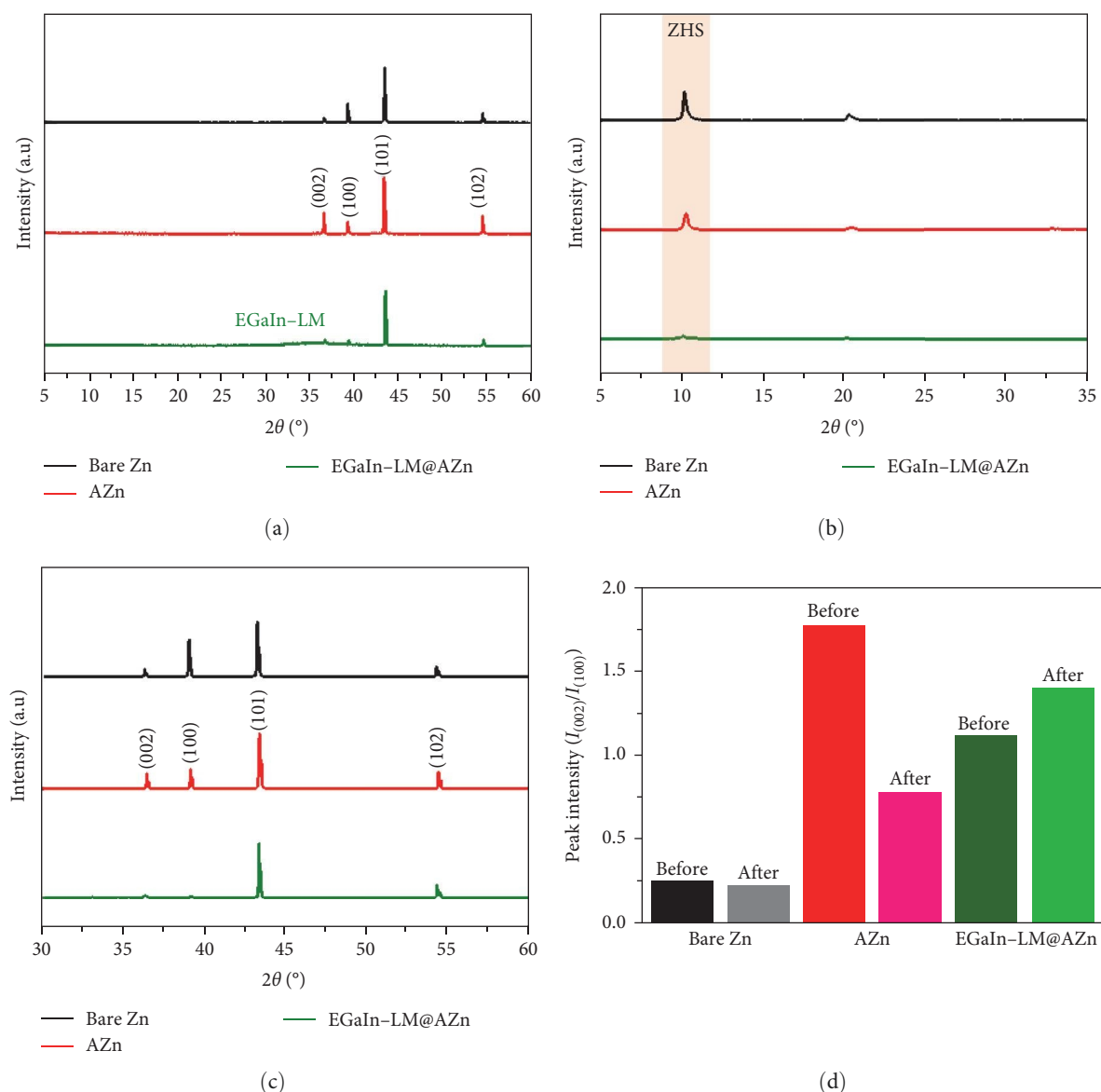
FIGURE 4: (a) XRD patterns of pristine bare Zn, AZn, and EGaIn–LM@AZn, (b) XRD patterns of soaked bare Zn, AZn, and EGaIn–LM@AZn in 2 M $ZnSO_4$ for 10 days, and (c) cycled bare Zn, AZn, and EGaIn–LM@AZn for 20 cycles at a current density of 1 mA cm^{-2} with areal capacity of 1 mAh cm^{-2}. (d) Peak intensity ratios of Zn (002) and Zn (100) of the pristine and cycled anodes.

byproducts, indicating that EGaIn–LM can inhibit the formation of these byproducts (Figure S5c). Next, we acquired the SEM images of the samples after 20 cycling tests under the same conditions as those used for XRD analysis (Figure S6). After the cycling tests, the Zn dendrites were randomly grown on the surface of the cycled bare Zn (Figure S6a). The cycled AZn also shows the growth of Zn dendrites; however, the Zn dendrites on the surface of AZn grew less randomly than those on the surface of the cycled bare Zn (Figure S6b). Unlike the cycled bare Zn and AZn, the surface of EGaIn–LM@AZn was clear and a negligible formation of Zn dendrites was observed (Figure S6c). These results indicate that the EGaIn–LM protective layer made Zn deposition uniform during the Zn plating and striping processes.

CE has been widely investigated to evaluate the Zn plating/stripping reversibility of Zn metal anode. Thus, we conducted CE tests for Cu//Zn half cells with different Zn anodes (Cu//bareZn, Cu//AZn and Cu//EGaIn–LM@AZn) with a current density of 1 mA cm^{-2} with an areal capacity of 1 mAh cm^{-2} (Figure 5). CE value of Cu//bare Zn and Cu//AZn half cells stated to fluctuate dramatically after 85 and 96 cycles, respectively, which indicated poor Zn plating/stripping reversibility caused by the formation of unfavored byproducts and dendrites. In contrast, CE value of Cu//EGaIn–LM@AZn half cell showed more outstanding CE stability without the fluctuation, compared to those of Cu//bare Zn and Cu//AZn, even after 200 cycles. Based on CE measurements, EGaIn–LM coating on AZn metal was beneficial to maintain stable Zn plating/stripping process against unfavored challenges in AZIBs such as byproducts, dendrites, HER, and corrosion.

To comprehensively evaluate the electrochemical performances of the anodes, we assembled AZIBs with V_2O_5 as a
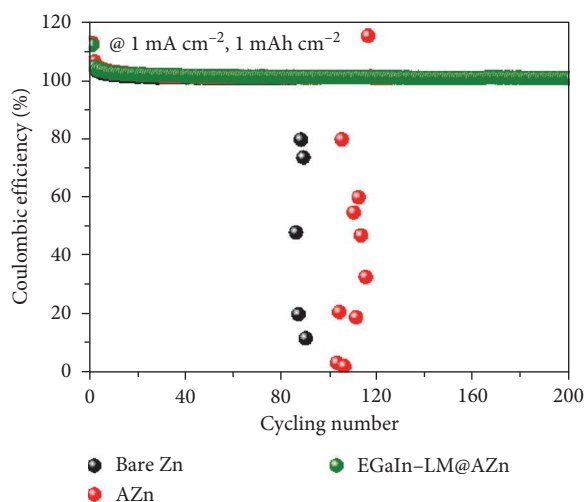
FIGURE 5: CE tests of Zn plating/stripping process on Cu//bare Zn, Cu//AZn, and Cu//EGaIn–LM@AZn under a current density of 1 mA cm^{-2} with a areal capacity of 1 mAh cm^{-2}.

cathode and the three different Zn anodes. The low interfacial charge transfer resistance owing to the liquid-to-liquid contact caused the V$_2$O$_5$//EGaIn–LM@AZn full cell to exhibit intensive peak currents and a large curve area at the same scan rate (0.4 mV s^{-1}), with respect to the V$_2$O$_5$//bare Zn and V$_2$O$_5$//AZn full cells (Figure S7). Additionally, these electrochemical behaviors continued at different scan rates between 0.2–1 mV s^{-1} (Figure 6a–c). At a scan rate of 0.2 mV s^{-1} in all three full cells, there is a reduction peak around 1.25 V since V$_2$O$_5$ exists in a metastable phase in aqueous electrolyte such as ZnSO$_4$ electrolyte, undergoing an activation process with a gradual capacity increase during the initial cycles. This process involves the intercalation of water molecules in to the V$_2$O$_5$ structure, resulting in interlayer expansion and phase transformation in to hydrated V$_2$O$_5$. This phase transformation reduces the Zn^{2+} diffusion barrier and enhances the structural stability during Zn^{2+} (de)intercalation [47, 48]. Prior to the completion of this phase transformation, the V$_2$O$_5$ cathode remains unstable, leading to the appearance of a reduction peak around 1.25 V at the initial scan rate during CV measurements. However, at followed scan rates, the reduction peak around 1.25 V diminishes, as shown in Figure 6a–c, meaning that V$_2$O$_5$ was stabilized. This phenomenon has been mentioned in many literatures based on V$_2$O$_5$–based cathode [47, 48]. Furthermore, we measured the interfacial charge transfer resistances of the full cells with different anodes via EIS analysis (Figure 6d). As shown in Figure 6d, the Nyquist plots of V$_2$O$_5$//EGaIn–LM@AZn indicated considerably lower interfacial charge transfer resistance than those of the other full cells, implying EGaIn–LM positively affected Zn-ion diffusion kinetics.

The charge/discharge profiles at various current densities between 0.2–5 A g^{-1} are displayed in Figure 7a–c. At a low current density of 0.2 A g^{-1}, the V$_2$O$_5$//bare Zn full cell exhibited a specific capacity of 417.7 mAh g^{-1}. Similarly, V$_2$O$_5$//AZn and V$_2$O$_5$//EGaIn–LM@AZn exhibited specific capacities of

427.6 and 422.4 mAh g^{-1}, respectively. The specific capacitance of V$_2$O$_5$//EGaIn–LM@AZn at a current density of 0.5 A g^{-1} was higher (466.8 mAh g^{-1}) than that at a current density of 0.2 A g^{-1} owing to the activation process that generally occurs in AZIBs. However, at a high current density of 5 A g^{-1}, the V$_2$O$_5$//EGaIn–LM@AZn full cell exhibited a specific capacity of 401.6 mAh g^{-1}, whereas V$_2$O$_5$//bare Zn and V$_2$O$_5$//AZn exhibited lower specific capacities of 301.9 and 310.2 mAh g^{-1}, respectively. At a current density of 5 A g^{-1}, the specific capacity of V$_2$O$_5$//EGaIn–LM@AZn was 1.33- and 1.29-times higher than that of V$_2$O$_5$//bare Zn and V$_2$O$_5$//AZn, respectively. Additionally, the specific capacities of V$_2$O$_5$//EGaIn–LM@AZn were more outstanding in overall current density conditions, compared to those of V$_2$O$_5$//bare Zn and V$_2$O$_5$//AZn. These results can be attributed to the improved charge transfer kinetics at the interface of the electrolyte and EGaIn–LM. The rate capability performances of the anodes were determined under various current densities to verify electrochemical stability when testing at a low current density after testing from a low to a high current density (Figure 7d). As shown in Figure 7d, even after testing at a high current density of 5 A g^{-1}, the V$_2$O$_5$//EGaIn–LM@AZn full cell exhibits a stable rate performance and the specific capacity on returning to the current density of 0.2 A g^{-1} is 484.7 mAh g^{-1}, whereas V$_2$O$_5$//bare Zn and V$_2$O$_5$//AZn exhibits specific capacities of 420.1 and 420.7 mAh g^{-1}, respectively.

To further investigate the stability during charge/discharge cycling tests, we conducted long-term charge/discharge measurements at current densities of 1 and 5 A g^{-1} over 250 and 1500 cycles, respectively (Figure 8a,b). As shown in Figure 8a, at a current density of 1 A g^{-1}, the V$_2$O$_5$//EGaIn–LM@AZn full cell maintains 50.1% of its initial specific capacity and yields 161.8 mAh g^{-1} after 250 cycles, whereas the V$_2$O$_5$//bare Zn and V$_2$O$_5$//AZn full cells exhibit 43.6% and 45.2% of the initial specific capacities and yield 132.8 and 135.6 mAh g^{-1}, respectively. Furthermore, even at a high current density of 5 A g^{-1} over 1500 cycles, the V$_2$O$_5$//EGaIn–LM@AZn full cell showed the highest cycling stability (71.8%) and the highest specific capacity (180 mAh g^{-1}), unlike the V$_2$O$_5$//bare Zn (53% and 115.7 mAh g^{-1}) and V$_2$O$_5$//AZn (55.0% and 120.2 mAh g^{-1}) full cells. Based on these results, as EGaIn–LM acted as a protective layer on Zn and improved anode stability, better long-term stabilities at current densities of 1 and 5 A g^{-1}, and rate capability performances were achieved than those of the full cells containing bare Zn and AZn anodes. These experiments involving anode symmetric cell and full cell measurements demonstrate that EGaIn–LM@AZn exhibited more outstanding electrochemical performance than bare Zn and AZn, indicating that simply brush coating EGaIn–LM on Zn improved the stability of Zn.

4. Conclusion

We designed a highly stable Zn anode for AZIBs by covering its surface with EGaIn–LM after acid treatment. Although acid treatment on Zn enhanced stability, EGaIn–LM@AZn exhibited substantial stability enhancement owing to the unique EGaIn–LM properties, including a liquid state, good wettability against the electrolyte, zincophilicity, and resistance to the HER
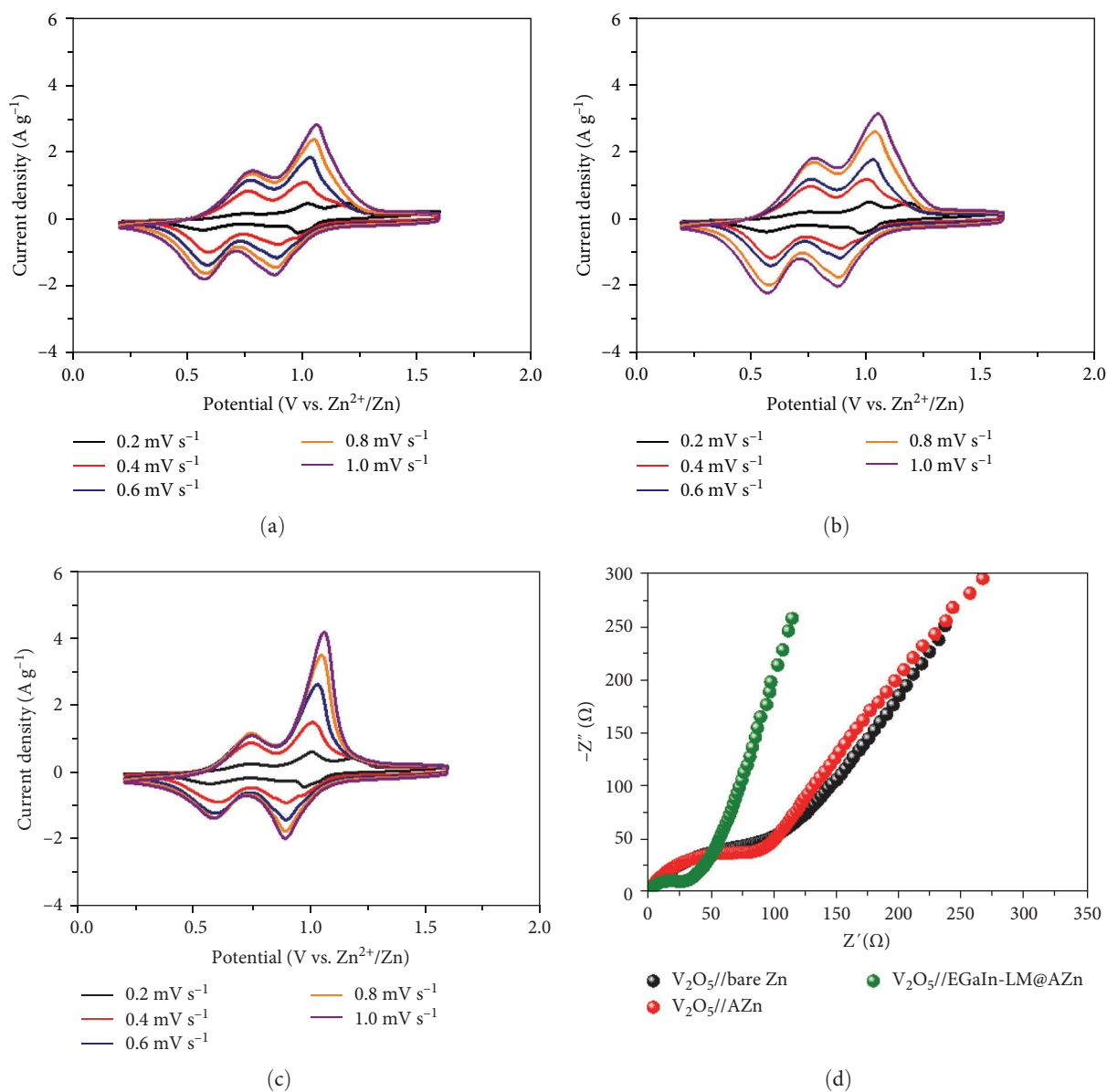
FIGURE 6: CV profiles of the full cells obtained under different scan rates: (a) V_2O_5//bare Zn, (b) V_2O_5//AZn, and (c) V_2O_5//EGaIn–LM@AZn. (d) EIS analysis.
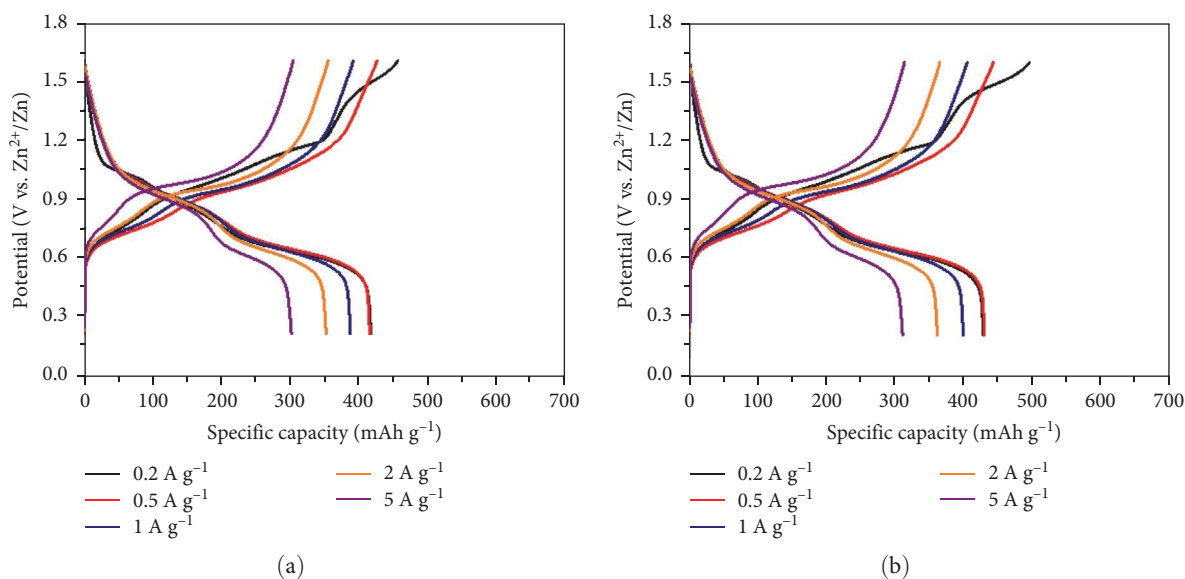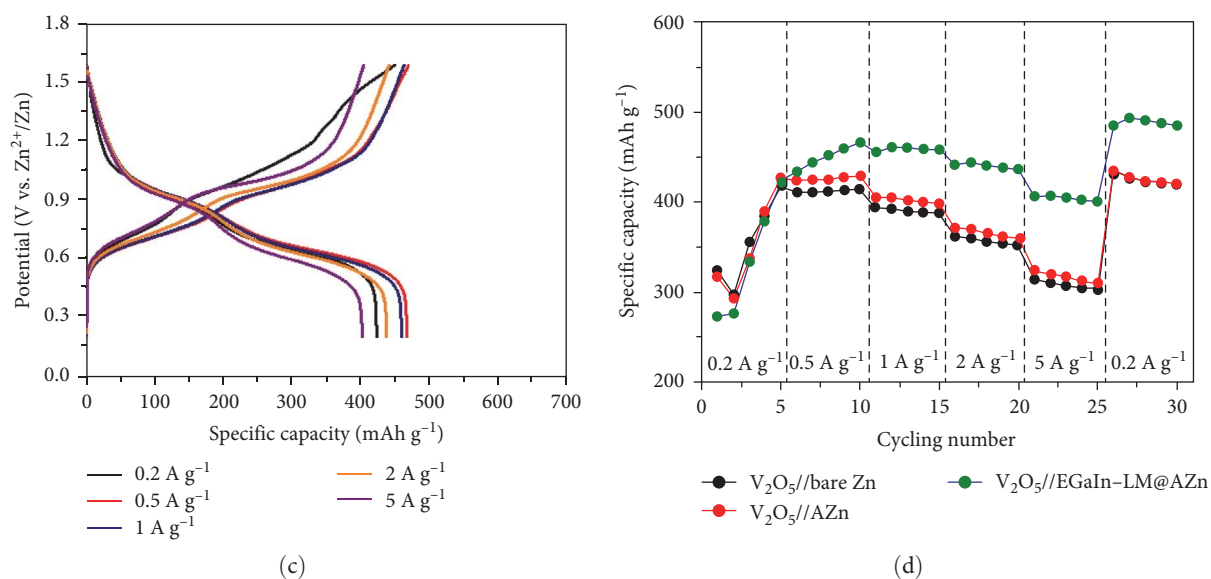

FIGURE 7: Continued.

(c)

(d)

FIGURE 7: Charge/discharge profiles at different current densities between 0.2–5 A g^{-1}: (a) V$_2$O$_5$//bare Zn, (b) V$_2$O$_5$//AZn, and (c) V$_2$O$_5$//EGaIn–LM@AZn. (d) Rate capability performances of the full cells with three different anodes.

(a)

(b)
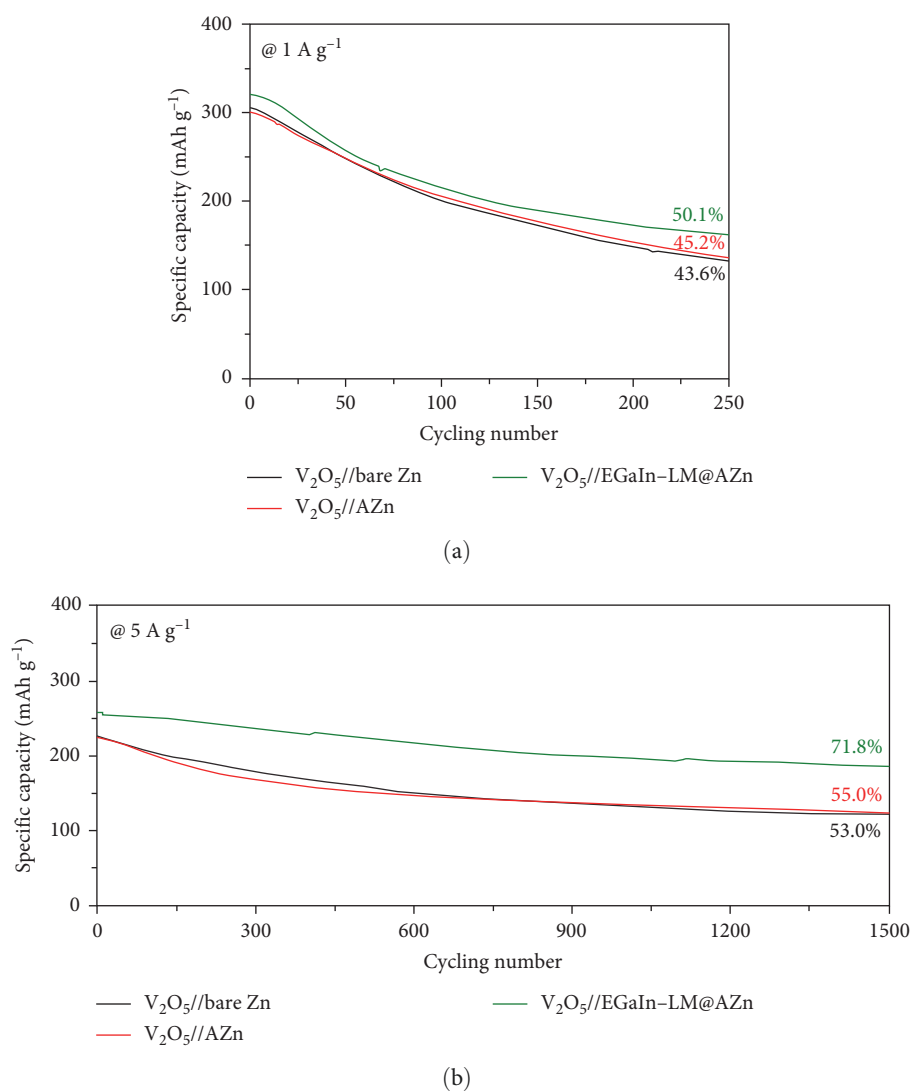
FIGURE 8: Long-term charge/discharge cycling tests conducted on V$_2$O$_5$//bare Zn, V$_2$O$_5$//AZn, and V$_2$O$_5$//EGaIn–LM@AZn at current densities of (a) 1 and (b) 5 A g^{-1}.

and corrosion. The EGaIn–LM@AZn anode significantly inhibited the formation of unfavorable ZHS byproducts and Zn dendrites, unlike in the case of the bare Zn and AZn anodes. Therefore, the EGaIn–LM@Zn anode exhibited more stable galvanostatic long-term cycling stability performance over 420 h. Furthermore, the V_2O_5//EGaIn–LM@AZn full cell showed stable rate capability, long-term charge/discharge cycling (capacity retention of 71.8% after 1500 cycles at a current density of 5 A g^{-1}), and high specific capacity under various current densities because of enhanced charge transfer kinetics and the protective ability of EGaIn–LM. Engineering the interface by simply brushing EGaIn–LM on Zn suggests a universal strategy to address the various obstacles related to Zn anodes. Therefore, the proposed process is promising for enhancing the stability of Zn in AZIBs.

Data Availability Statement

The data that support the findings of this study are available from the corresponding author upon reasonable request.

Conflicts of Interest

The authors declare no conflicts of interest.

Author Contributions

Hyungsub Yoon: conceptualization, formal analysis, investigation, visualization, writing–original draft. Chunghyeon Choi: formal analysis, investigation, visualization, writing–original draft. Seungwoo Hong: formal analysis. Marita Afiandika: formal analysis, investigation, visualization, writing–original draft. Aleksandar Matic: supervision, conceptualization, formal analysis, investigation, writing–original draft, writing–review and editing. Tae Gwang Yun: supervision, formal analysis, investigation, writing–original draft, writing–review and editing. Byungil Hwang: conceptualization, formal analysis, investigation, project administration, supervision, writing–original draft, writing–review and editing.

Supporting Information

Additional supporting information can be found online in the Supporting Information section. (*Supporting Information*) Figure S1 shows the photographs of bare Zn, AZn, EGaIn-LM@bare Zn, and EGaIn-LM@AZn. Figure S2 exhibits the contact angle measurements of the three different anodes with 2 M $ZnSO_4$ electrolyte. Figure S3 shows the enlarged XRD patterns of EGaIn-LM@AZn between 20–50°. Figures S4, S5, and S6 display the SEM images of the pristine, soaked in an electrolyte, and cycled bare Zn, AZn, and EGaIn-LM@AZn anodes, respectively. Figure S7 shows the CV profiles at a scan rate of 0.4 mV s^{-1} according to V_2O_5–based full cells with bare Zn, AZn, and EGaIn-LM@AZn anodes. Table S1 shows a comparison of a galvanostatic long-term cycling stability of Zn symmetric cell with different coating materials.

References

[1] T. Suryaprabha, T. Kiruthika, P. Selvamurugan, et al., "Recycling Primary Batteries into Advanced Graphene Flake-Based Multifunctional Smart Textiles for Energy Storage, Strain Sensing, Electromagnetic Interference Shielding, Antibacterial, and Deicing Applications," *Journal of Cleaner Production* 479 (2024): 144020.

[2] G. Li, "Regulating Mass Transport Behavior for High-Performance Lithium Metal Batteries and Fast-Charging Lithium-Ion Batteries," *Advanced Energy Materials* 11 (2021): 2002891.

[3] Y. Yang, E. G. Okonkwo, G. Huang, S. Xu, W. Sun, and Y. He, "On the Sustainability of Lithium Ion Battery Industry-A Review and Perspective," *Energy Storage Materials* 36 (2021): 186–212.

[4] Y. Zhao, L. Wang, Y. Zhou, et al., "Solid Polymer Electrolytes With High Conductivity and Transference Number of Li Ions for Li-Based Rechargeable Batteries," *Advanced Science* 8, no. 7 (2021): 2003675.

[5] W. Leng, L. Cui, Y. Liu, and Y. Gong, "MOF-Derived MnV_2O_4/C Microparticles With Graphene Coating Anchored on Graphite Sheets: Oxygen Defect Engaged High Performance Aqueous Zinc-Ion Battery," *Advanced Materials Interfaces* 9 (2022): 2101705.

[6] S. Wei, S. Chen, X. Su, et al., "Manganese Buffer Induced High-Performance Disordered MnVO Cathodes in Zinc Batteries," *Energy & Environmental Science* 14 (2021): 3954–3964.

[7] T. Yan, S. Liu, J. Li, et al., "Constructing a Topologically Adaptable Solid Electrolyte Interphase for a Highly Reversible Zinc Anode," *ACS Nano* 18, no. 4 (2024): 3752–3762.

[8] Q. Nian, X. Luo, D. Ruan, et al., "Highly Reversible Zinc Metal Anode Enabled by Strong Brønsted Acid and Hydrophobic Interfacial Chemistry," *Nature Communications* 15 (2024): 4303.

[9] X. Cai, W. Tian, Z. Zhang, et al., "Polymer Coating With Balanced Coordination Strength and Ion Conductivity for Dendrite-Free Zinc Anode," *Advanced Materials* 36, no. 3 (2024): e2307727.

[10] N. Guo, Z. Peng, W. Huo, et al., "Stabilizing Zn Metal Anode Through Regulation of Zn Ion Transfer and Interfacial Behavior With a Fast Ion Conductor Protective Layer," *Small* 19, no. 47 (2023): e2303963.

[11] T. Wang, P. Wang, L. Pan, et al., "Stabling Zinc Metal Anode With Polydopamine Regulation Through Dual Effects of Fast

Desolvation and Ion Confinement," *Advanced Energy Materials* 13 (2023): 2203523.

[12] J. Wang, Z. Zhao, F. Hu, et al., "Highly Reversible Zn Metal Anodes Enabled by Multifunctional Poly Zinc Acrylate Protective Coating," *Chemical Engineering Journal* 451 (2023): 139058.

[13] Y. Liu, Y. Ding, Z. Liu, et al., "Ultrafast Laser One-Step Construction of 3D Micro-/Nanostructures Achieving High-Performance Zinc Metal Anodes," *PhotoniX* 5 (2024): 6.

[14] D. Meng, X. Liang, Q. Liu, et al., "An Electrostripping Strategy for Constructing a 3D Honeycomb-Like Zn Anode Toward Dendrite-Free Zinc-Ion Batteries," *Advanced Functional Materials* 34 (2024): 2411047.

[15] M. Chen, M. Yang, X. Han, J. Chen, P. Zhang, and C. P. Wong, "Suppressing Rampant and Vertical Deposition of Cathode Intermediate Product via PH Regulation Toward Large-Capacity and High-Durability $Zn//MnO_2$ Batteries," *Advanced Materials* 36 (2024): 2304997.

[16] J. Chen, M. Chen, H. Chen, et al., "Wood-Inspired Anisotropic Hydrogel Electrolyte With Large Modulus and Low Tortuosity Realizing Durable Dendrite-Free Zinc-Ion Batteries," *Proceedings of the National Academy of Sciences of the United States of America* 121, no. 21 (2024): e2322944121.

[17] Y. Song, P. Ruan, C. Mao, et al., "Metal-Organic Frameworks Functionalized Separators for Robust Aqueous Zinc-Ion Batteries," *Nano-Micro Letters* 14, no. 1 (2022): 218.

[18] H. Ma, H. Chen, M. Chen, et al., "Biomimetic and Biodegradable Separator With High Modulus and Large Ionic Conductivity Enables Dendrite-Free Zinc-Ion Batteries," *Nature Communications* 16, no. 1 (2025): 1014.

[19] Y. Yin, S. Wang, Q. Zhang, et al., "Dendrite-Free Zinc Deposition Induced by Tin-Modified Multifunctional 3D Host for Stable Zinc-Based Flow Battery," *Advanced Materials* 32, no. 6 (2020): 1906803.

[20] S.-B. Wang, Q. Ran, R.-Q. Yao, et al., "Lamella-Nanostructured Eutectic Zinc-Aluminum Alloys as Reversible and Dendrite-Free Anodes for Aqueous Rechargeable Batteries," *Nature Communications* 11, no. 1 (2020): 1634.

[21] J. Zhou, M. Xie, F. Wu, et al., "Ultrathin Surface Coating of Nitrogen-Doped Graphene Enables Stable Zinc Anodes for Aqueous Zinc-Ion Batteries," *Advanced Materials* 33, no. 33 (2021): 2101649.

[22] X. Wang, J. Meng, X. Lin, et al., "Stable Zinc Metal Anodes With Textured Crystal Faces and Functional Zinc Compound Coatings," *Advanced Functional Materials* 31, no. 48 (2021): 2106114.

[23] Y. Mu, T. Zhou, D. Li, et al., "Highly Stable and Durable Zn-Metal Anode Coated by Bi-Functional Protective Layer Suppressing Uncontrollable Dendrites Growth and Corrosion," *Chemical Engineering Journal* 430 (2022): 132839.

[24] S. Jia, H. Bian, B. Wang, et al., "Synergistic Long-Term Protection of Inorganic and Polymer Hybrid Coatings for Free-Dendrite Zinc Anodes," *Langmuir* 40, no. 47 (2024): 25143–25153.

[25] D. Y. Jeong, W. J. Chang, S. Jang, et al., "Controlling Dendrite Growth and Side Reactions in Anode-Free Zn-Ion Aqueous Batteries With PMMA: Zn Coated Electrode," *Journal of Energy Storage* 76 (2024): 109791.

[26] Z. Zhao, H. Zhang, X. Shi, et al., "Zincophilic Metal-Organic-Framework Interface Mitigating Dendrite Growth for Highly Reversible Zinc Metal Batteries," *Small* 20, no. 6 (2024): 2304723.

[27] J. He, W. Zhou, J. Li, S. Chen, D. Zhu, and Y. Chen, "Bifunctional Interface of Metal-Organic Framework Synergized With Bismuth Endows High Stable Zinc Anode," *Chemical Engineering Journal* 485 (2024): 149740.

[28] K. Yun and G.-H. An, "Surface Protection and Nucleation Enhancement of Zinc Anode With Graphene and Doped Carbon Nanotubes for High-Performance Energy Storage," *Chemical Engineering Journal* 479 (2024): 147303.

[29] Q.-P. Bao, Z. Li, B.-B. Sui, et al., "Highly Stable Planted MXene Auxiliary Layer for High-Performance Zinc Anode Deposition Regulation," *Chemical Engineering Journal* 496 (2024): 154345.

[30] K. Wang, J. Hu, T. Chen, et al., "Interface Engineering of Flexible Liquid Metal Modulation To Achieve Dendrite-Free Zinc Metal Anodes," *ACS Sustainable Chemistry & Engineering* 11, no. 24 (2023): 9111–9120.

[31] H. Chen, Z. Guo, H. Wang, W. Huang, F. Pan, and Z. Wang, "A Liquid Metal Interlayer for Boosted Charge Transfer and Dendrite-Free Deposition Toward High-Performance Zn Anodes," *Energy Storage Materials* 54 (2023): 563–569.

[32] J. Pu, Q. Cao, Y. Gao, et al., "Liquid Metal-Based Stable and Stretchable Zn-Ion Battery for Electronic Textiles," *Advanced Materials* 36, no. 2 (2024): 2305812.

[33] C. Liu, Z. Luo, W. Deng, et al., "Liquid Alloy Interlayer for Aqueous Zinc-Ion Battery," *ACS Energy Letters* 6, no. 2 (2021): 675–683.

[34] S. Hong, Z. Choi, B. Hwang, and A. Matic, "Research Trends and Future Perspectives on Zn-Ion Batteries Using Ga-Based Liquid Metal Coatings on Zn Anodes," *ACS Energy Letters* 9, no. 11 (2024): 5421–5433.

[35] J.-H. Kim, S. Kim, H. Kim, et al., "Imbibition-Induced Selective Wetting of Liquid Metal," *Nature Communications* 13, no. 1 (2022): 4763.

[36] H. Kim, G. Kim, J. H. Kang, M. J. Oh, N. Qaiser, and B. Hwang, "Intrinsically Conductive and Highly Stretchable Liquid Metal/Carbon Nanotube/Elastomer Composites for Strain Sensing and Electromagnetic Wave Absorption," *Advanced Composites and Hybrid Materials* 8, no. 1 (2025): 1–14.

[37] J. Zou, Z. Zeng, C. Wang, X. Zhu, and J, "Zhang Ultraconformal Horizontal Zinc Deposition Toward Dendrite-Free Anode," *Small Structures* 4, no. 1 (2023): 2200194.

[38] J. Cao, X. Wang, S. Qian, et al., "De-Passivation and Surface Crystal Plane Reconstruction via Chemical Polishing for Highly Reversible Zinc Anodes," *Advanced Materials* 36, no. 46 (2024): 2410947.

[39] Y. Du, Y. Feng, R. Li, et al., "Zinc-Bismuth Binary Alloy Enabling High-Performance Aqueous Zinc Ion Batteries," *Small* 20, no. 17 (2024): 2307848.

[40] J. Cao, X. Wang, D. Zhang, et al., "Pre-Corrosion of Zinc Metal Anodes for Enhanced Stability and Kinetics," *Small* 20, no. 43 (2024): 2403622.

[41] G. Li, Z. Liu, Q. Huang, et al., "Stable Metal Battery Anodes Enabled by Polyethylenimine Sponge Hosts by Way of Electrokinetic Effects," *Nature Energy* 3, no. 12 (2018): 1076–1083.

[42] M. Zhang, W. Xu, X. Han, et al., "Unveiling the Mechanism of the Dendrite Nucleation and Growth in Aqueous Zinc Ion Batteries," *Advanced Energy Materials* 14, no. 9 (2024): 2303737.

[43] Y. Hao, D. Feng, L. Hou, T. Li, Y. Jiao, and P. Wu, "Gel Electrolyte Constructing Zn (002) Deposition Crystal Plane

Toward Highly Stable Zn Anode," *Advanced Science* 9, no. 7 (2022): 2104832.

[44] M. M. Alsaif, F. Haque, T. Alkathiri, et al., "3D Visible-Light-Driven Plasmonic Oxide Frameworks Deviated From Liquid Metal Nanodroplets," *Advanced Functional Materials* 31, no. 52 (2021): 2106397.

[45] H. Liu, H. Deng, S. Liu, et al., "Maltose Additive Enables Compacted Deposition of Zn Ions for Stabilizing the Zn Anode," *ACS Applied Materials & Interfaces* 16, no. 27 (2024): 35217–35224.

[46] D. Xie, Z. W. Wang, Z. Y. Gu, et al., "Polymeric Molecular Design Towards Horizontal Zn Electrodeposits at Constrained 2D Zn^{2+} Diffusion: Dendrite-Free Zn Anode for Long-Life and High-Rate Aqueous Zinc Metal Battery," *Advanced Functional Materials* 32 (2022): 2204066.

[47] R. Li, H. Zhang, Q. Zheng, and X. Li, "Porous V_2O_5 Yolk-Shell Microspheres for Zinc Ion Battery Cathodes: Activation Responsible for Enhanced Capacity and Rate Performance," *Journal of Materials Chemistry A* 8 (2020): 5186–5193.

[48] K. Zhu, T. Wu, and K. Huang, "Understanding the Dissolution and Phase Transformation Mechanisms in Aqueous Zn/α-V_2O_5 Batteries," *Chemistry of Materials* 33 (2021): 4089–4098.